Electromechanically Reconfigurable Terahertz Stereo Metasurfaces

Saurav Prakash[1,7], Prakash Pitchappa[2*], Piyush Agrawal[3,4], Hariom Jani[1,5], Yunshan Zhao[6], Abhishek Kumar[3,4], John Thong[6], Jian Linke[1], Ariando Ariando[1,7], Ranjan Singh[3,4*], Thirumalai Venkatesan[6,8*]

[1]*Department of Physics, National University of Singapore, Singapore 117551*

[2]*Institute of Microelectronics (IME), Agency for Science, Technology and Research (A*STAR), 2 Fusionopolis Way, Singapore 138634*

[3]*Division of Physics and Applied Physics, School of Physical and Mathematical Sciences, Nanyang Technological University, 21 Nanyang Link, Singapore-637371*

[4]*Centre for Disruptive Photonic Technologies, The Photonic Institute, 50 Nanyang Avenue, Singapore-639798*

[5]*Clarendon Laboratory, Department of Physics, University of Oxford, Oxford, UK OX13PU*

[6]*Department of Electrical and Computer Engineering, National University of Singapore, Singapore 117583*

[7]*NUS Graduate School for Integrative Science and Engineering, National University of Singapore, Singapore-117456*

[8]*Center for Quantum Research and Technology (CQRT), Center of Optimal Materials for Emerging Technologies (COMET) University of Oklahoma, Oklahoma, US 73019*

**email*: *venky@ou.edu; ranjans@ntu.edu.sg; prakash_pitchappa@ime.a-star.edu.sg*

Abstract

Dynamic terahertz devices are vital for the next generation of wireless communication, sensing and non-destructive imaging technologies. Metasurfaces have emerged as a paradigm-shifting platform, offering varied functionalities, miniaturization and simplified fabrication compared to their three-dimensional counterparts. However, the presence of in-plane mirror symmetry and reduced degree of freedom imposes fundamental limitations on achieving advanced chiral response, beamforming, and reconfiguration capabilities. In this work, we demonstrate a platform composed of electrically actuated resonators that can be colossally reconfigured between planar and 3D geometries. To illustrate the platform, metadevices with 3D Split Ring Resonators have been fabricated wherein we combine two counteracting driving forces – (i) folding induced by stress mismatch which enables non-volatile state design, and (ii) unfolding triggered by the strain associated with insulator-to-metal transition in VO_2, which facilitates volatile structural reconfiguration. This large structural reconfiguration space allows for resonance mode switching, widely tunable magnetic and electric polarizabilities, and increased frequency agility. Moreover, the unique properties of VO_2 such as the hysteretic nature of its phase transition is harnessed to demonstrate a multi-state memory. Therefore, these VO_2 integrated metadevices are highly attractive for the realization of 6G communication devices such as reconfigurable intelligent surfaces, holographic beam formers, and spatial light modulators.

Keywords

vanadium dioxide, phase-change, metasurfaces, terahertz, MEMS

Introduction

The terahertz (THz) region of the electromagnetic spectrum (0.1-10 THz) has numerous promising applications, including the next generation (6G) of high-speed wireless communication, spectroscopy, and imaging[1]. It lies between the infrared and the microwave spectral regions and is often referred to as the 'THz gap' due to the lack of functional THz devices. This is primarily due to the scarcity of natural materials exhibiting strong electric or magnetic responses/polarizabilities in THz frequencies. On this front, the advent of metasurfaces, the 2D equivalent of metamaterial, has arguably been the most important development for realizing efficient functional THz devices. Metasurfaces are engineered materials consisting of an array of sub-wavelength resonators, whose electromagnetic properties are predominantly determined by the shape/geometry of the resonator. By designing resonators with specific shapes, metasurfaces with exotic THz responses have been reported, including artificial magnetism[2], negative refractive index[3], strong chirality[4], and perfect absorption[5]. However, once fabricated, the response of the metasurface remains fixed which severely limits its adoption in real-world applications. Consequently, over the past decade, extensive effort has been devoted to realizing dynamic THz metasurfaces, also known popularly as 'metadevices', that can have their response tuned, switched, and/or reconfigured through the application of external stimuli.

Broadly there are two approaches for creating THz metadevices – (i) incorporating active materials within the resonator structure or as the surrounding media, and (ii) structural reconfiguration of the resonator shape and/or orientation. The former approach has been used extensively to realize a myriad of planar THz metadevices by integrating various types of active materials including phase-change materials[6], semiconductors[7], 2D materials[8], liquid crystals[9] and superconductors[10]. However, these active material-integrated THz metadevices are generally planar, not spectrally scalable, often have limited tunability, suffer from inherent

losses, and/or require bulky and power-intensive driving stimuli. Alternatively, micro-electromechanical system (MEMS) integrated THz metadevices exhibiting in-plane and out-of-plane structural reconfiguration have been shown to deliver advanced functionalities, enhanced performance, miniaturization, and/or energy efficiency[11]. However, most of these reported out-of-plane reconfigurable metadevices using conventional MEMS actuators are limited to small deflections on a portion of a predominantly 2D resonator (typical length to deformation ratio ~ 0.1), resulting in a quasi-3D structure[12]. Due to the small structural reconfiguration space, the nature of interaction with THz waves and polarizability of the conventional MEMS-integrated THz resonators, remains mostly unchanged. Complete access to the third dimension by forming truly 3D resonators is therefore crucial for accessing new paradigms of light-matter interaction, especially by promoting strong interaction with the magnetic field of the normally incident THz waves. Additionally, it expands the structural reconfiguration space allowing for resonance mode switching, increased frequency agility, which ultimately broadens their scope for translation. Metasurfaces with truly 3D resonators, referred to as 'stereo' metasurfaces[11b, 13], have the potential to unlock functionalities such as negative refractive index, chirality, and toroidal excitations, that are usually not achievable with conventional MEMS-integrated THz metasurfaces. Although, passive THz stereo metasurfaces have been realized using extremely complicated fabrication approaches[14], their functionality remains fixed upon fabrication. Building upon their own work on passive 3D resonators, Fan et al. demonstrated limited tunability by exploiting the photoconductivity of the Si patch in the capacitive gap of the 3D SRRs[15]. However, the discussed devices are not structurally reconfigurable, resulting in them sharing the same limitations as active material integrated THz metadevices, including requiring an energy expensive bulky laser. Realizing stereo (3D) metasurfaces with structurally reconfigurable resonators for the THz spectrum has been a major challenge. Few demonstrations have shown the potential of dynamically opening up of the third dimension, resulting in enhanced chirality and resonance switching[11a, 16]. However, these devices rely on

pneumatic actuation and high temperature annealing, which are not integration friendly, energy expensive and/or only allow for one-time reconfiguration.

Here, we report a scalable VO_2-based platform to realize electromechanically reconfigurable THz stereo metadevices. We have used two counteracting yet complementary actuating forces for colossal and multifunctional structural reconfiguration of 3D THz resonators; one is the stress-mismatch induced folding which enables non-volatile structural changes, and another is strain related to the insulator-to-metal transition (IMT) in VO_2, which enables volatile changes in the resonator's structure. The reconfiguration of the devices is also accomplished electrically, facilitating high degree of miniaturization and integration. Additionally, we show multi-state memory effect using sub-threshold transient electrical stimulus that leverages the hysteretic nature of IMT in VO_2. Even though a plethora of VO_2 integrated THz planar metadevices have been reported exploiting the dielectric property change across IMT in VO_2, in this work, we harness the large strain associated with IMT in VO_2, while the change in dielectric property of VO_2 across the IMT is largely inconsequential. Therefore, we are able to preserve the desirable functional attributes of VO_2, such as the memory effect, in our devices while avoiding detrimental effects such as resonance weakening due to the intertwined nature of change in permittivity and conductivity in the VO_2 material system[6b]. Our platform with rich array of functionalities has an immense potential to realize functional THz devices such as reconfigurable intelligent surfaces, holographic beam formers, and spatial light modulators for the future 6G communication networks.

Results

Scheme for Electromechanically Reconfigurable THz Stereo Metadevice

To illustrate the platform, we have fabricated metadevices with the 3D split-ring resonators (SRRs). **Figure 1a** shows the schematic of the THz stereo metadevice with an array of 3D SRRs.

The two material layers forming the 3D SRR structure are Aluminum (Al) and VO_2. The fabrication process is elaborated in section III of Supporting Information (SI). After the device fabrication, the bimaterial cantilevers are curved up due to the residual stress between the two material layers, forming the 3D SRR structure with radius (r) and corresponding gap (g). In order to achieve reconfiguration from this initial 3D state to a 2D state, we exploit the colossal recoverable strain associated with IMT in VO_2, as shown schematically in **Figure 1b and 1c**. Since the reconfiguration is achieved though current driven Joule heating, a unique "U-shaped" design is adopted for the arms of the 3D SRR. It ensures that the current applied between the rectangular bond pads goes through the arms (see **Figure 1a**). This enables relatively low current powered reconfiguration of the devices by facilitating localized heating of VO_2 underneath the current carrying Al layer.

The THz waves are incident normal to the metadevice with the electric field along x-direction (E_x) and the magnetic field along y-direction (H_y) as shown in Figure 1. In the 3D SRR state, the electric field E_x lies perpendicular to the gap and the magnetic field H_y lies perpendicular to the plane of the SRR. Hence, both E_x and H_y of the incident THz wave would drive circulating current in the SRR loop, resulting in the excitation of a magnetic dipole m_y **(**see **Figure 1b)** alongside an electric dipole along the gap (x-direction). Contrarily, in the planar state, an oscillating current is induced along the 2D cantilever predominantly due to the electric field E_x (see **Figure 1c)**, resulting in the excitation of an electric dipole only. Hence, the transformation of a resonator from a fully 3D to a planar 2D geometry allows for switching of the nature of resonant excitation from a strongly magnetic to an electric one. In addition to switching the resonators between these extremities, the percolative nature of phase transition in VO_2[17], enables access to a continuum of intermediate configurations. Hence, the proposed multifunctional platform allows for spectrally tunable magnetic and electric polarizabilities in the THz region necessary for advanced beam forming applications[18].

Geometrically Defined Reconfiguration Space

The Al and VO_2 bimaterial cantilever explored in this work attains a well-defined radius of curvature that minimizes the potential energy of the entire structure. This is a commonly observed phenomenon in stress mismatched bimaterial cantilever upon release from the substrate[19] (see SI section I for further details). As a result, the structural reconfiguration space of the metadevice fabricated using this platform can be predictably designed by appropriately choosing the 2D precursor. For achieving the 3D split ring structure with gap on top, the 2D precursor was chosen as a 200 μm long planar U-shaped cantilever on either side of the anchor (see SI Figure S2a). Therefore, all the possible structures of resonator are defined by the relation, $r \times \theta = L_c$, where r is the radius of curvature, θ is the sector angle and L_c is the total length of cantilever structure (400 μm), also represented by the red curve in **Figure 2a** (see schematic in SI Figure S2b). Inset on either side of **Figure 2a** shows a representative structure at the two extremities. For $\theta \geq 180°$, the 3D split ring description with radius (r) and corresponding gap (g) is applied. For $\theta < 180°$, the bent cantilever description with deflection (δ) from the substrate is applied (see SI Figure S2c and S2d). Table S1 (see SI section II) shows the list of feasible structures with their simulated resonant frequency. The bimaterial cantilever can be structurally reconfigured continuously from the 3D split ring to a completely flat 2D cantilever, provided we have a means to engineer the stress mismatch between the Al and VO_2 layer. This large structural reconfiguration of the resonator geometry triggers a notable shift in resonant frequency of the metadevice as represented by the green curve shown in **Figure 2a** (see also Table S1 in SI). As the 3D SRR structure starts unfolding, the resonant frequency first blue-shifts sharply and then steadily, but eventually a non-monotonic red-shift is observed. The SRR geometry can be modeled as an array of RLC elements and its resonance frequency $\omega = \left(L_{eff}C_{eff}\right)^{(-1/2)}$, where the effective inductance *(L_{eff})* results from the current path of the SRR and the effective capacitance *(C_{eff})* is determined by the gap dimensions and self-capacitance[20].

The sharp blue-shift initially is due to $1/g$ dependence of the gap capacitance. As the gap becomes larger the gap capacitance becomes insignificant, the continued blue shift is predominantly due to decreasing inductance of the structure going from a ring like to a planar geometry. In this phase of evolution, the resonant frequency blue shifts almost linearly with decreasing sector angle, θ. The linear extrapolation of this would have resulted in a 2D structure with resonant frequency ~ 0.53 THz (intercept of the dashed line in **Figure 2a**). However, due to the proximity to the high index Si substrate, the resonant frequency red shifts owing to the increased capacitance between the cantilever and the substrate.

The entire structural reconfiguration space can therefore be divided into 2 regions based on the structure classification discussed previously, see **Figure 2a**. This also signifies that predominant physical interaction of THz waves and the resonant response in each of the regions are widely different. In order to elucidate this observation, the magnetic and electric field strength were calculated at resonance, for three representative structures with sector angle (θ) 355°, 180° and 30°. The normalized magnetic field (**Figure 2b-2d**) and electric field (**Figure 2e-2g**) are shown at the respective resonant frequency for the three structures. Strong magnetic and electric field enhancement is observed for the 3D SRR geometry, i.e., θ=355° as shown in **Figure 2b and 2e**, respectively. As the structure unfolds, i.e., θ=180°, the strength of fields reduces considerably (see **Figure 2c and 2f**, respectively). At θ=30°, the structure resembles that of a 2D cantilever, and hence only a weak field enhancement is observed at resonant frequency. This is due to the transition from a strongly magnetic polarizability in the 3D SRR situation to a predominantly electric polarizability in the 2D cantilever. Such a switching between resonance modes can also be discerned from the resonant lineshape broadening as the resonator transitions into a flat structure, see SI figure S3. This is due to the increased radiation damping for the bent cantilever geometry, due to suppression of magnetic dipole response in

favor of electric dipole response, also seen in the field profiles discussed earlier[21]. In the following sections, we demonstrate the versatility of a single VO_2 MEMS metadevice proposed in this research. It allows for tunable magnetic response in Region 1, switching between magnetic and electrical response, and tunable electrical response in Region 2. Utilizing this VO_2 MEMS platform, we can predictably produce a variety of 3D resonators from a 2D precursor, with colossally reconfigurable THz response. Our simulation results are confirmed through experimental observations, which are further detailed in the subsequent sections.

Non-Volatile Electromechanical Reconfiguration

The use of VO_2 for micromechanical devices has been limited to devices with a few actuators so far, and the translation to a large periodic array remains challenging[22]. This is mainly due to the need for large anchor pads to prevent the complete removal of the sacrificial layer from underneath it. Moreover, the material combinations and their thicknesses used in the reported devices, are not suited to support strong resonances in THz spectral range. Due to these limitations, a VO_2-based structurally reconfigurable dynamic THz metasurface has not been achievable thus far. We have developed a robust and scalable microfabrication process (see SI Figure S4) to achieve large area samples with high yield, which is a critical requirement for THz metadevices. The details of the fabrication process are provided in section III of the SI. Individual steps were optimized to facilitate the creation of 3D structures, and to be able to switch to planar geometries i.e., large actuation amplitude. Some representative 3D test structures fabricated using the optimized process are shown in SI Figure S6.

To experimentally illustrate the platform, we have fabricated a metadevice featuring 3D SRRs as discussed previously. The dimensions of the 2D cantilever precursor which transforms into 3D SRR is shown in SI Figure S2a. Three metadevices TG1, TG2 and TG3 were fabricated identically up to step VII of SI Figure S4 but were eventually treated with different current-driven rapid annealing step. Left panel of **Figure 3a-c** shows the top view SEM images of

fabricated 3D SRR metadevices TG1, TG2 and TG3 subjected to currents 250 mA, 275 mA and 300 mA for 30s, respectively. The gaps for TG1, TG2 and TG3 are estimated to be 110 µm, 33 µm and 1µm, respectively, with a corresponding radius of 83 µm, 69 µm and 64 µm as shown in the right panel of **Figure 3a-c**. As the precursor is subject to increasing currents post release, the residual stress in the bimaterial layers gets modified causing the radius of curvature to decrease, i.e., folding to increase, which results in 3D SRRs with a smaller gap. The THz response of the fabricated metadevices is measured using THz time-domain spectroscopy (see methods for further details). The normalized THz transmission through the metadevices shows a pronounced dip at the resonant frequency of 0.394 THz, 0.345 THz and 0.256 THz for TG1, TG2 and TG3, respectively as shown in **Figure 3d**. While we have used three samples to illustrate this non-volatile reconfiguration aspect, the same device can be set in progressively folded 3D states by successively increasing annealing current magnitude and/or duration.

To elucidate the interaction of THz waves with the metadevices, simulations were performed using CST Microwave Studio, wherein average structural parameters extracted from SEM images were used to define the SRR dimensions. While the experimental resonant frequency agrees reasonably well with the simulation results shown in **Figure 3e**, it is relatively weaker and broader. This broadening arises mainly due to the fabrication related non-uniformities. As discussed, for the 3D SRR metadevices with the gap on top (see **Figure 1b**), both magnetic field (perpendicular to loop) and electric field (perpendicular to the gap) drive a circulating current resulting in the excitation of a magnetic dipole[16b]. To highlight the versatility of our fabrication approach, we fabricated a 3D SRR metadevice with the gap located in the side arm as shown in SI Figure S7. The dimensions of the equivalent 2D cantilever which transforms into 3D SRR with gap in the side arm is shown in Figure S7a. The resonant response of this device is driven purely by the magnetic field (H_y) of the incident THz waves as the electric field (E_x) is parallel to the gap. Figure S7c and S7d show the THz response of this metadevice and the induced current at resonance respectively. In essence, exploiting stress mismatch induced

folding, we can fabricate metadevices with 3D SRRs, whose structural characteristics i.e., radius, gap and location of the gap can be electromechanically set in a non-volatile manner. As a result, it is possible to design the resonant frequency and the nature of polarizability, allowing for programming of the electromagnetic space dynamically with zero hold power.

Volatile Electromechanical Reconfiguration through Phase transition in VO_2

The adoption of VO_2 as one of the structural layers for our devices allows for large and reversible electromechanical reconfiguration of the metadevices, in addition to the non-volatile functionality discussed above. Across the IMT, VO_2 undergoes a structural phase transition from the insulating monoclinic phase to the metallic rutile phase as shown in the inset of SI Figure S8a. The strain associated with this phase transition unfolds the structure enabling dynamic access to the entire structural reconfiguration space.

Current dependent THz transmission measurements were performed by mounting the sample onto a chip carrier and making electrical connections to the bond pads on the device (see methods for further details). **Figure 4a** shows the resonant frequency of the metadevice TG2 as the current is ramped up, and subsequently ramped down. The hysteretic nature of IMT in VO_2 is also observed in the THz response of the device. The gradual non-hysteretic portion of the curve is presumably due to the structural reconfiguration caused by difference in thermal expansion coefficients of VO_2 and Al. Whereas the steep hysteretic region is predominantly due to large strain associated with the crystallographic phase[22a] change during the IMT in VO_2. To validate this attribution, we performed systematic temperature dependent THz measurements of the metadevice (see SI Figure S8). We find that the abrupt hysteretic response corresponds well with the IMT observed in the DC resistance measurements of a continuous VO_2 film, confirming that the THz response is indeed related to the phase transition in VO_2.

Figure 4b shows the THz transmission through the metadevices for different applied currents. As the current ramps up, the resonant frequency first blue shifts from 0.35 to ~ 0.372 (260 mA)

and then to ~ 0.504 (267 mA) THz. Thereafter, it red shifts to ~ 0.4 THz (276 mA). This non-monotonic response corresponds well with the simulation results discussed previously, in **Figure 2**. The abrupt broadening of the resonant lineshape across the IMT is also seen in **Figure 4b**. As discussed, this is due to increased radiation damping associated with the electric nature of resonance in the bent cantilever state [21a, 23]. SEM images and supplementary movie 1 reveal the extent of structural reconfiguration, and its reversible nature when the driving current is switched off. Across the IMT, the 3D SRR structure unfolds, and transitions into a nearly flat 2D cantilever as shown in **Figure 4c (i)-(v)**. It should be noted that the current driven reconfiguration depends significantly on the thermal properties of the environment which inhibits direct correlation between experimentally measured structure and resonant response for the TG2 metadevice. Hence, a lower current ~ 120 mA is required to drive IMT during SEM experiment (performed in vacuum) compared to ~ 276 mA during THz spectroscopy (performed in a continuous nitrogen purge). Despite these minor differences, the evolution of structure and THz response for the TG2 metadevice measured experimentally corresponds well to its simulated counterparts.

Multi-state Memory due to Hysteretic Phase Transition in VO_2

As discussed in the previous section, the metadevice inherits the hysteretic IMT behavior of VO_2 (see **Figure 4a** and SI Figure S8b). Therefore, our metadevices also function as an electrically controlled memory. We have used metadevice TG3 (see **Figure 3**) to demonstrate this memory effect as shown in **Figure 5**. The threshold transient stimulus required to switch ON the device completely was identified (see SI Table S3). Control experiments were also performed to identify Switch ON time and Reset time of the device for these transient current stimuli. The operation speed of the device is therefore limited by the reset time, i.e. the time required for the VO_2 layer to transition back to the monoclinic phase. Thermal management strategies to accelerate the heat loss will be required to further boost the operation speed to sub

kHz level[24] (see section VII of SI for further detail). Subsequently, subthreshold transient current stimulus is applied to demonstrate a multi-state memory effect.

The device was first pushed into the hysteretic regime by applying a constant 'Read' current of 250 mA as shown in the lower panel of **Figure 5a and 5b**. Thereafter, 'Write' current pulses were applied while the change in THz response of the device was monitored. The transient current stimulus is characterized by the magnitude of current (I) and temporal width (Δt). **Figure 5a** shows the multi-state response of the device after 'Write' current pulses are applied with fixed temporal width (Δt = 200 milliseconds) but increasing magnitude of current. Each 'Write' step in this case is followed by an 'Erase' step whereby the 'Read' current is switched off, i.e. I = 0 mA. Upon arrival of the 'Write' pulse, the resonant frequency blue shifts, and this change in resonant frequency persists even after the transient excitation is over provided the 'Read' current is not switched off. The modified resonant state was monitored for 30s post transient stimulus and did not show any sign of degradation. Previous reports on the DC memory resistance of VO_2 suggest that the effect will persist much longer[25]. The extent of the blue shift is proportional to the magnitude of write current given the temporal width of the excitation is identical. Additionally, we have also studied the device response upon excitation with a series of identical sub-threshold 'Write' pulses keeping the delay between them at 2 seconds, which is lower than the measured Reset time (~ >12 s) shown in SI Figure S10. Plots in red and green in **Figure 5b** shows the response of the device for serially applied 'Write' pulses of 400 mA, Δt = 500 ms and 600 mA, Δt = 100 ms, respectively. With each arriving pulse, the resonant frequency of the device progressively blue shifts as expected. Here, the number of 'Write' pulses applied serially and the delay between them determines the state of the device. Therefore, a multi-state memory with varying resonant states is achieved using sub-threshold transient current stimulus.

Conclusion

We have presented an electrically controlled platform to realize structurally reconfigurable metasurfaces featuring 3D resonators in the THz regime. Our fabrication approach allowed us to successfully demonstrate a metadevice with 3D SRRs, whose structural parameters can be set in a non-volatile manner by a current driven annealing treatment, post fabrication. Additionally, we showcase the colossal volatile reconfiguration of the resonator from the 3D SRR configuration to the planar 2D cantilever configuration facilitated by IMT in VO_2. The large structural reconfiguration space enables giant frequency agility and switching of resonant response from a strongly magnetic to an electric one. Furthermore, we exploited the percolative and hysteretic nature of the IMT in VO_2 to reversibly access a continuum of intermediate states and to demonstrate multi-state memory, respectively. The platform is promising as it enables the engineering of electromagnetic space in multifunctional way, paving the way towards functional THz devices in the field of wireless communication, such as reconfigurable intelligent surfaces, holographic beam formers, and spatial light modulators.

Experimental Section

Numerical simulations. Full-wave electromagnetic simulations were performed using Computer Software Technology (CST) Microwave Studio, a commercial finite integration package. A unit cell of the device structure is simulated using periodic boundary conditions. We have used the frequency domain solver option which is based on the finite difference time domain (FDTD) method. For the material property, aluminum (Al) was modelled as a lossy metal with a DC conductivity of 3.56×10^7 S/m and silicon substrate with a dielectric constant of 11.7.

THz Characterization. We used Picometrix, T-Ray 4000 Terahertz Time-Domain Spectrometer for metadevice characterization. Samples were mounted on a chip carrier with a square aperture for electromechanical experiments. DC current dependent THz response

measurements were performed by slowly increasing/decreasing the applied current in steps. Picostream feature of the spectrometer was used to perform time resolved experiments. LabVIEW program to control Keithley 2400 SMU was used to apply electrical stimulus. Temperature dependent THz measurements were carried out in a cryostat.

Supporting Information

Supporting Information is available from the Wiley Online Library or from the author.

Acknowledgements

This work was supported by the Science and Engineering Research Council of A*STAR (Agency for Science, Technology and Research) Singapore, under Grant No. M22L1b0110. We would also like to thank Dr. Sonu Hooda and Dr. Ganesh Ji Omar for the helpful discussions. S.P. and P.P. conceived and designed the study, carried out the modeling of metadevices, conducted the device fabrication, and performed material, THz, and electrical characterizations. P.A. and H.J. assisted with the temporal THz measurement experiment. Y.Z. and J.T. assisted with current-driven scanning electron microscopy characterizations. A.K. assisted with THz set up and measurements. J.L. helped with the microfabrication. S.P. wrote the manuscript with input from all authors. T.V., R.S., A.A., and P.P. supervised the whole project. All authors analyzed the data and discussed the results.

Received: ((will be filled in by the editorial staff))
Revised: ((will be filled in by the editorial staff))
Published online: ((will be filled in by the editorial staff))

References

[1] a)T. S. Rappaport, Y. Xing, O. Kanhere, S. Ju, A. Madanayake, S. Mandal, A. Alkhateeb, G. C. Trichopoulos, *IEEE access* **2019**, 7, 78729; b)M. Tonouchi, *Nature Photonics* **2007**, 1, 97; c)F. Yang, P. Pitchappa, N. Wang, *Micromachines* **2022**, 13, 285; d)B. Ferguson, X.-C. Zhang, *Nature materials* **2002**, 1, 26; e)R. Al Hadi, H. Sherry, J. Grzyb, Y. Zhao, W. Forster, H. M. Keller, A. Cathelin, A. Kaiser, U. R. Pfeiffer, *IEEE Journal of Solid-State Circuits* **2012**, 47, 2999; f)T. Nagatsuma, G. Ducournau, C. C. Renaud, *Nature Photonics* **2016**, 10, 371; g)K. Sengupta, T. Nagatsuma, D. M. Mittleman, *Nature Electronics* **2018**, 1, 622.

[2] T. J. Yen, W. J. Padilla, N. Fang, D. C. Vier, D. R. Smith, J. B. Pendry, D. N. Basov, X. Zhang, *Science* **2004**, 303, 1494.

[3] S. Zhang, Y.-S. Park, J. Li, X. Lu, W. Zhang, X. Zhang, *Physical Review Letters* **2009**, 102, 023901.

[4] E. Philip, M. Zeki Güngördü, S. Pal, P. Kung, S. M. Kim, *Journal of Infrared, Millimeter, and Terahertz Waves* **2017**, 38, 1047.

[5] a)C. Chen, M. Chai, M. Jin, T. He, *Advanced Materials Technologies* **2022**, 7, 2101171; b)Y. Zhao, Q. Huang, H. Cai, X. Lin, Y. Lu, *Optics Communications* **2018**, 426, 443.

[6] a)A. Mandal, Y. Cui, L. McRae, B. Gholipour, *Journal of Physics: Photonics* **2021**; b)T. Driscoll, H.-T. Kim, B.-G. Chae, B.-J. Kim, Y.-W. Lee, N. M. Jokerst, S. Palit, D. R. Smith, M. Di Ventra, D. N. Basov, *Science* **2009**, 325, 1518; c)P. Pitchappa, A. Kumar, S. Prakash, H. Jani, T. Venkatesan, R. Singh, *Advanced Materials* **2019**, 31, 1808157.

[7] a)M. Manjappa, Y. K. Srivastava, L. Cong, I. Al‐Naib, R. Singh, *Advanced Materials* **2017**, 29, 1603355; b)H.-T. Chen, W. J. Padilla, J. M. Zide, A. C. Gossard, A. J.

Taylor, R. D. Averitt, *Nature* **2006**, 444, 597; c)H.-T. Chen, J. F. O'hara, A. K. Azad, A. J. Taylor, R. D. Averitt, D. B. Shrekenhamer, W. J. Padilla, *Nature Photonics* **2008**, 2, 295.

[8] a)Q. Li, X. Cai, T. Liu, M. Jia, Q. Wu, H. Zhou, H. Liu, Q. Wang, X. Ling, C. Chen, *Nanophotonics* **2022**, 11, 2085; b)S. H. Lee, M. Choi, T.-T. Kim, S. Lee, M. Liu, X. Yin, H. K. Choi, S. S. Lee, C.-G. Choi, S.-Y. Choi, *Nature materials* **2012**, 11, 936.

[9] a)G. Isić, B. Vasić, D. C. Zografopoulos, R. Beccherelli, R. Gajić, *Physical Review Applied* **2015**, 3, 064007; b)J. Xu, R. Yang, Y. Fan, Q. Fu, F. Zhang, *Frontiers in Physics* **2021**, 9, 633104.

[10] a)O. Limaj, F. Giorgianni, A. Di Gaspare, V. Giliberti, G. De Marzi, P. Roy, M. Ortolani, X. Xi, D. Cunnane, S. Lupi, *Acs Photonics* **2014**, 1, 570; b)J. Gu, R. Singh, Z. Tian, W. Cao, Q. Xing, M. He, J. W. Zhang, J. Han, H.-T. Chen, W. Zhang, *Applied Physics Letters* **2010**, 97; c)G. R. Keiser, J. Zhang, X. Zhao, X. Zhang, R. D. Averitt, *JOSA B* **2016**, 33, 2649.

[11] a)P. Pitchappa, A. Kumar, R. Singh, C. Lee, N. Wang, *Journal of Micromechanics and Microengineering* **2021**; b)Y. Xu, Q. Xu, X. Zhang, X. Feng, Y. Lu, X. Zhang, M. Kang, J. Han, W. Zhang, *Advanced Functional Materials* **2022**, 32, 2207269.

[12] a)L. Cong, P. Pitchappa, C. Lee, R. Singh, *Advanced materials* **2017**, 29, 1700733; b)M. Manjappa, P. Pitchappa, N. Singh, N. Wang, N. I. Zheludev, C. Lee, R. Singh, *Nature communications* **2018**, 9, 4056.

[13] Z. Liu, Y. Xu, C. Y. Ji, S. Chen, X. Li, X. Zhang, Y. Yao, J. Li, *Advanced Materials* **2020**, 32, 1907077.

[14] a)D. B. Burckel, P. J. Resnick, P. S. Finnegan, M. B. Sinclair, P. S. Davids, *Optical Materials Express* **2015**, 5, 2231; b)D. B. Burckel, J. R. Wendt, G. A. Ten Eyck, A. R. Ellis, I. Brener, M. B. Sinclair, *Advanced Materials* **2010**, 22, 3171; c)K. Fan, W. J. Padilla, *Materials Today* **2015**, 18, 39.

[15] K. Fan, A. C. Strikwerda, X. Zhang, R. D. Averitt, *Physical Review B* **2013**, 87, 161104.

[16] a)T. Kan, A. Isozaki, N. Kanda, N. Nemoto, K. Konishi, H. Takahashi, M. Kuwata-Gonokami, K. Matsumoto, I. Shimoyama, *Nature Communications* **2015**, 6, 8422; b)H. Tao, A. Strikwerda, K. Fan, W. Padilla, X. Zhang, R. Averitt, *Physical review letters* **2009**, 103, 147401; c)H. Tao, A. C. Strikwerda, K. Fan, W. J. Padilla, X. Zhang, R. D. Averitt, *Journal of Infrared, Millimeter, and Terahertz Waves* **2011**, 32, 580.

[17] M. M. Qazilbash, M. Brehm, B.-G. Chae, P.-C. Ho, G. O. Andreev, B.-J. Kim, S. J. Yun, A. Balatsky, M. Maple, F. Keilmann, *Science* **2007**, 318, 1750.

[18] C. Pfeiffer, A. Grbic, *Physical review letters* **2013**, 110, 197401.

[19] a)J.-N. Kuo, G.-B. Lee, W.-F. Pan, H.-H. Lee, *Japanese journal of applied physics* **2005**, 44, 3180; b)Z. Liu, A. Cui, J. Li, C. Gu, *Advanced materials* **2019**, 31, 1802211; c)E. Moiseeva, Y. Senousy, S. McNamara, C. Harnett, *Journal of Micromechanics and Microengineering* **2007**, 17, N63.

[20] a)J. D. Baena, J. Bonache, F. Martín, R. M. Sillero, F. Falcone, T. Lopetegi, M. A. Laso, J. Garcia-Garcia, I. Gil, M. F. Portillo, *IEEE transactions on microwave theory and techniques* **2005**, 53, 1451; b)G. V. Eleftheriades, O. Siddiqui, A. K. Iyer, *IEEE Microwave and Wireless Components Letters* **2003**, 13, 51.

[21] a)G. Della Valle, T. Søndergaard, S. I. Bozhevolnyi, *Physical Review B* **2009**, 79, 113410; b)A. Pors, M. Willatzen, O. Albrektsen, S. I. Bozhevolnyi, *JOSA B* **2010**, 27, 1680.

[22] a)V. Balakrishnan, C. Ko, S. Ramanathan, *Journal of Materials Research* **2011**, 26, 1384; b)J. Cao, W. Fan, Q. Zhou, E. Sheu, A. Liu, C. Barrett, J. Wu, *Journal of Applied Physics* **2010**, 108, 083538; c)C. Huang, Z. Zhang, S. Ramanathan, D. Weinstein, *IEEE Transactions on Electron Devices* **2019**, 66, 4380; d)K. Liu, C. Cheng, Z. Cheng, K. Wang, R. Ramesh, J. Wu, *Nano letters* **2012**, 12, 6302; e)E. Merced, D. Torres, X. Tan, N. Sepúlveda, *Journal of Microelectromechanical Systems* **2014**, 24, 100; f)A. Rúa, F. E. Fernández, N. Sepúlveda, *Journal of Applied Physics* **2010**, 107, 074506; g)D. Torres, S. Dooley, L. V. Starman, N. Sepúlveda, presented at *Mechanics of Biological Systems & Micro-*

and Nanomechanics, Volume 4: Proceedings of the 2018 Annual Conference on Experimental and Applied Mechanics, **2019**.

[23] G. Della Valle, T. Søndergaard, S. I. Bozhevolnyi, *Physical Review B* **2009**, 80, 235405.

[24] R. Cabrera, E. Merced, N. Sepúlveda, *Journal of microelectromechanical systems* **2013**, 23, 243.

[25] T. Driscoll, H.-T. Kim, B.-G. Chae, M. Di Ventra, D. Basov, *Applied physics letters* **2009**, 95, 043503.

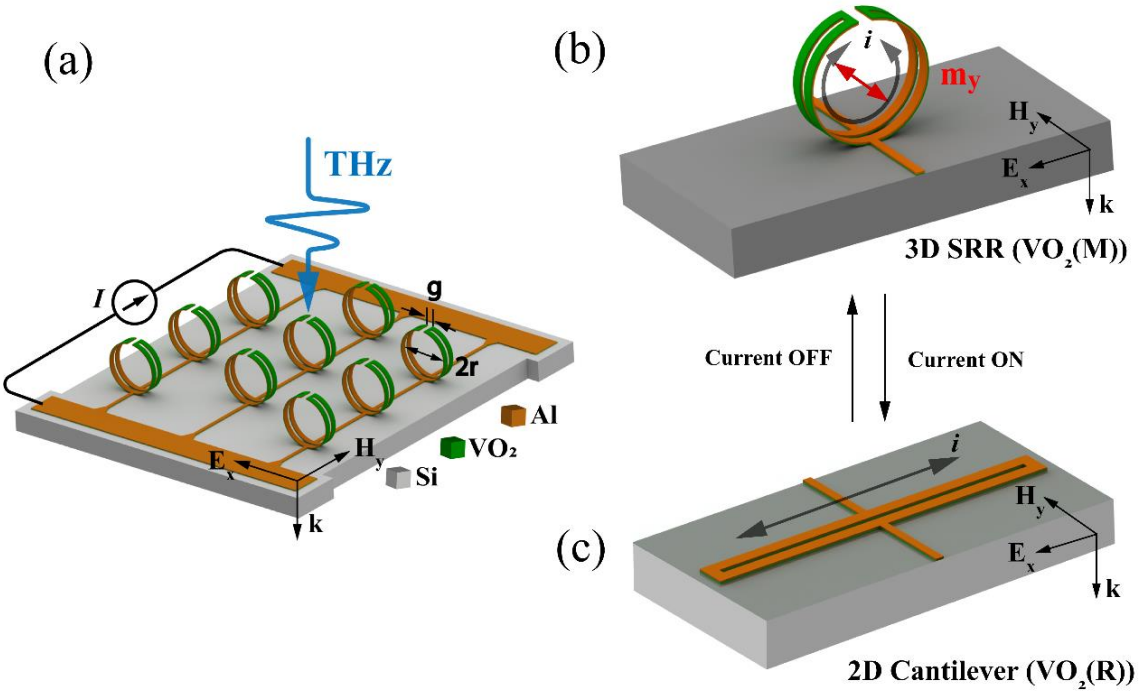

Figure 1. (a) Scheme of VO_2 integrated electromechanically reconfigurable metadevice featuring 3D SRRs with radius *r* and gap *g*. Bond pads for the application of electric currents and the polarization of the incident THz radiation are also shown. **(b)** Magnified schematic of the 3D SRR showing the induced circulating current, *i*, (black arrow) at resonance, resulting magnetic dipole moment m_y (red arrow). Switching on the external current, *I*, drives a phase transition in VO_2 causing actuation of the structure into a 2D cantilever configuration. **(c)** Schematic showing the planar 2D cantilever with the induced current, *i*, (black arrow) at resonance, resulting in the excitation of an electric dipole primarily.

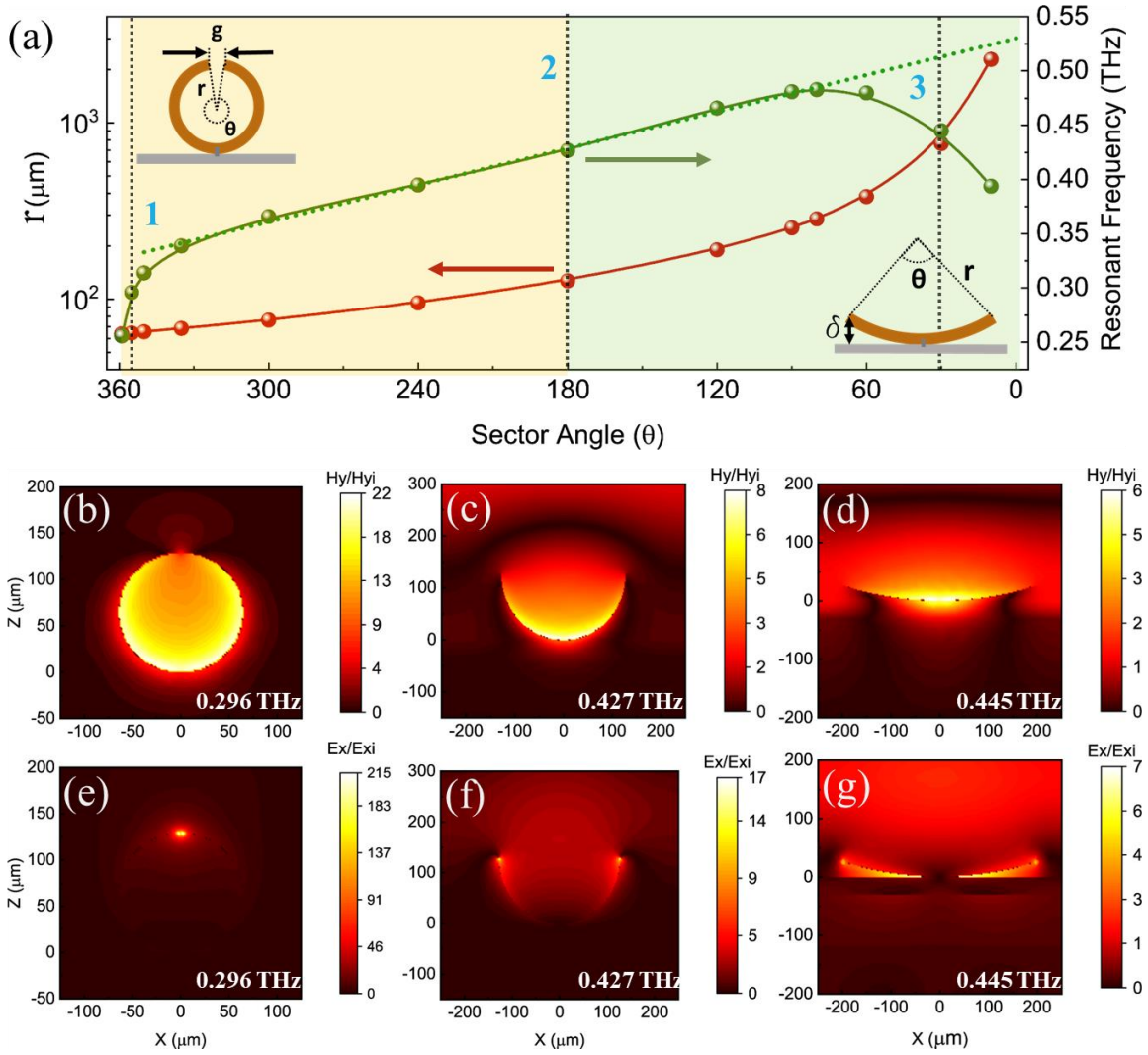

Figure 2. Geometrically defined structural reconfiguration space. **(a)** Possible resonator structures that can be realized by continuously folding a 400 μm long flat cantilever. The red curve represents the calculated radius of curvature of the folded structure, and the green curve represents the simulated resonant frequency for the corresponding structure. Simulated normalized magnetic **(b-d)** and electric field distribution **(e-g)** at the resonant frequency for three configurations identified as 1, 2 and 3 (*dashed lines*) in **(a)**.

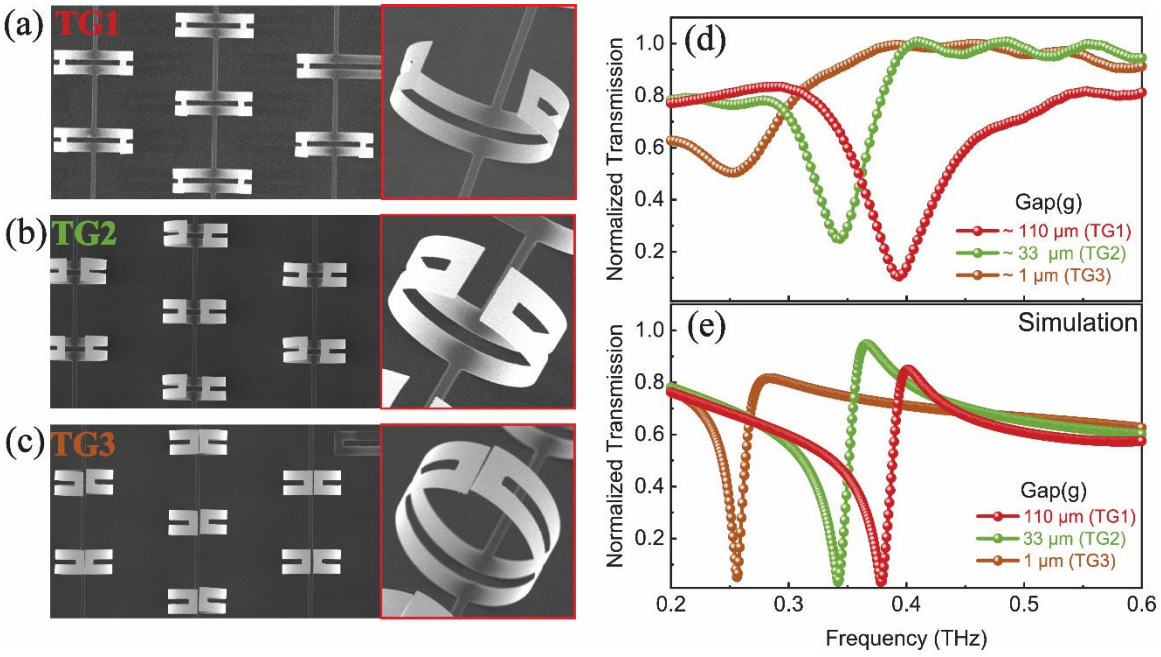

Figure 3. Non-volatile electromechanical reconfiguration through stress mismatch induced folding. Top view SEM images of 3D SRR array (*left panel*) and magnified SEM image of a single SRR unit (*right panel*) for three metadevices **(a)** TG1, **(b)** TG2 and **(c)** TG3. Non-volatile reconfiguration current for the devices TG1, TG2 and TG3 are 250 mA, 275 mA and 300 mA respectively. **(d)** Measured and **(e)** simulated THz transmission through devices TG1, TG2 and TG3. Average gap for devices TG1, TG2 and TG3 (estimated from the SEM images) are 110 μm, 33 μm and 1 μm, respectively.

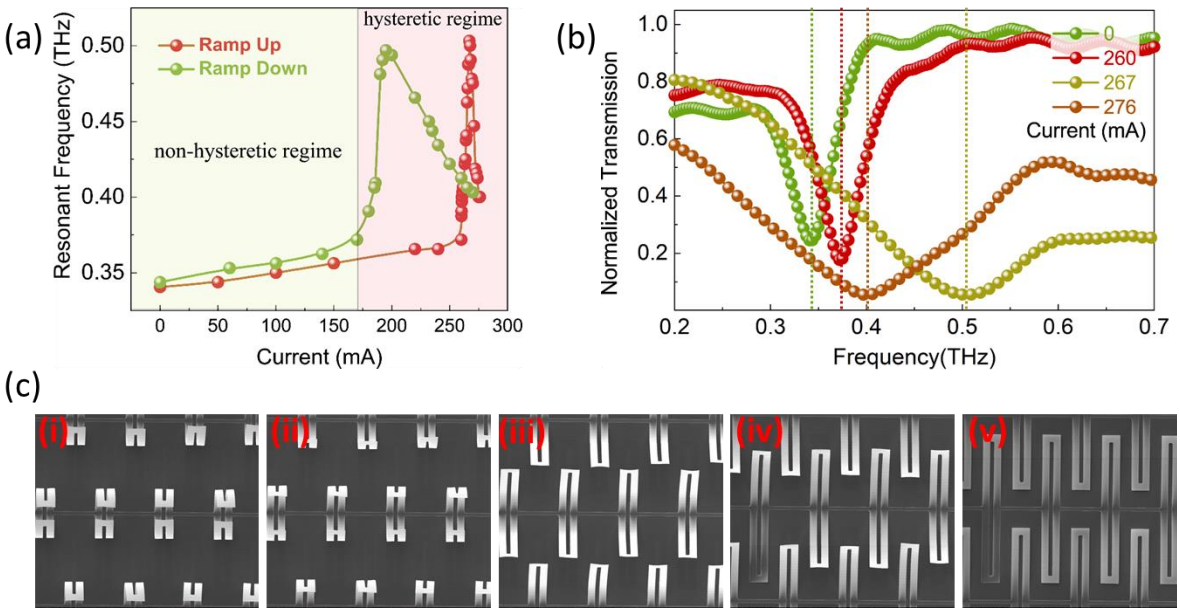

Figure 4. Volatile electromechanical reconfiguration through IMT in VO_2. (a) Resonant frequency of the THz metadevice TG2 as steady-state current is ramped – up (red curve) and down (green curve). **(b)** Snapshots of normalized THz transmission for a few current values (0, 260 mA, 267 mA and 276 mA) during the current ramp up leg. Dotted lines identify the resonant frequency at respective current values. **(c)** *In situ* top view SEM images of the device as the current is increased. As the VO_2 is driven across the IMT, the structures gradually transition from 3D SRRs to nearly planar 2D cantilevers. Increasing current from left to right.

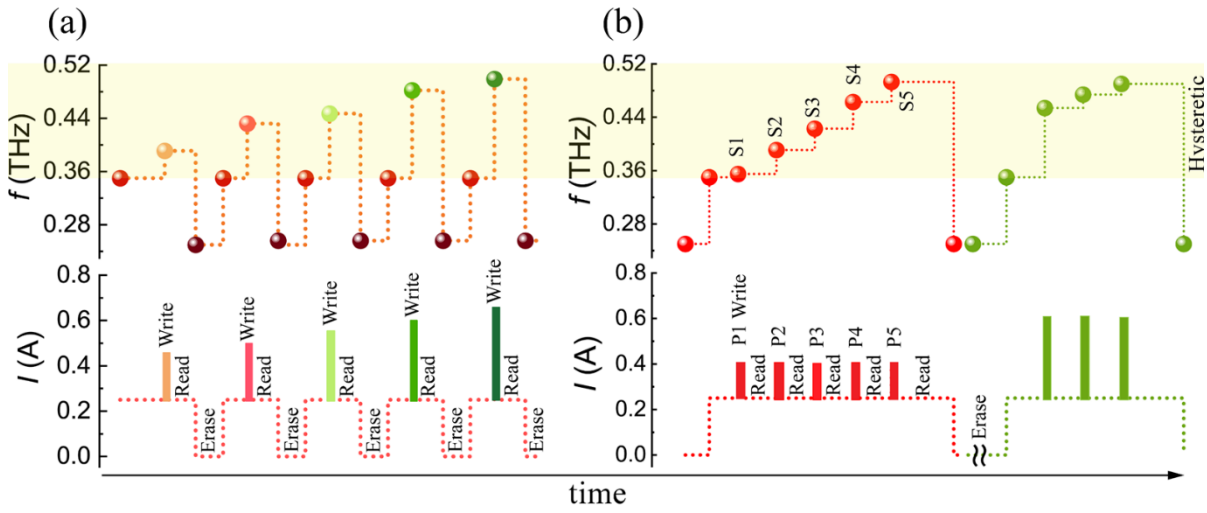

Figure 5. Multi-state memory metadevice. (a) *(lower panel)* Transient write current (fixed pulse width Δt ~ 200 ms) with increasing magnitude applied to metadevice TG3 followed by steady state 'read' current (250 mA) and 'erase' step (0 mA). (*upper panel*) Corresponding persistent change in the resonant frequency of metadevice. **(b)** (*lower panel*) sequential pulsing of the same transient stimulus and the corresponding resonant frequency response of the device (*upper panel*). (Red curve) Sequential pulses (labeled P1-P5, without the erase cycle) with a magnitude and temporal width of 400 mA and 500 ms resulting in 5 discernible persistent states (labeled S1-S5) in the frequency range 0.35 THz (onset of hysteretic regime) and 0.5 THz. (Green curve) Sequential pulses with a magnitude and width of 600 mA and 100 ms results in three discernible persistent states. Delay between sequential write pulses is 2s.